Enhancing the Security of Geologic Carbon Storage

Using Coated Silicate Nanoparticles

Tyler Brown

B.S. Civil Engineering, University of Virginia 2018

A Thesis presented to the Graduate Faculty

of the University of Virginia in Candidacy for the Degree of
Master of Science

Civil and Environmental Engineering

Engineering Systems and Environment, University of Virginia

May 2019

Andres F. Clarens (advisor)

Lisa M. Colosi-Peterson

James A. Smith

Abstract

The large-scale deployment of geologic carbon storage has been hindered by several factors including the risk of CO_2 leakage. Here we report on the development of functionalized reactive nanoparticles that could be co-injected with the CO_2 to seal flow pathways that might lead to large scale leakage. The nanoparticles, consisting of a mineral silicate core coated with a temperature-sensitive polydopamine shell, are unreactive at high temperatures near the injection site but become reactive at the lower temperatures that would prevail near leakage zones. Once the core material comes in contact with aqueous CO_2, it will react to form calcium or magnesium carbonate precipitates that reduce the permeability of the fracture or flow path. Functionalized nanoparticles containing calcium silicate ($CaSiO_3$) cores were synthesized and coated before being injected into sand columns. Above the critical temperature for the coatings, the permeability drops were modest but below the critical temperature, much more significant drops were observed. SEM-EDS and synchrotron μXRD and μXRF were used to characterize the morphology and location of the precipitates to demonstrate that they could would effectively block fluid flow even at relatively low nanoparticle concentrations far from the injection well. A model of nanoparticle transport was developed to provide insight into the effect of nanoparticle size, coating properties, and concentrations in various representative formations.

Table of Contents

1 Introduction

Geologic carbon sequestration (GCS) has been proposed as an important strategy for meeting near-term efforts for providing carbon-neutral energy even though the potential exists for CO_2 to leak from target formations deep in the subsurface. These leakage events could represent a safety risk if CO_2 migrates from its target repository in the subsurface, damaging nearby hydrocarbon or freshwater reservoirs or escaping to the atmosphere. Leaks to the atmosphere would undermine the motivation for GCS (Bohnhoff and Zoback, 2010). Most studies to date suggest that fractures, fissures and degraded materials associated with wellbores and natural faults and fractures in the subsurface present the greatest risk for leakage (Bruant et al., 2002; Nordbotten et al., 2004). Even though the aggregate risks of leakage from CO_2 injection sites will not be fully known until more pilot facilities are built, the unprecedented scale of fluid injection and long-term permanent storage required to meaningfully avert carbon emissions demands the development of scalable technologies capable of sealing leakage pathways and mitigating leakage risk (IPCC, 2014). When considered along with the persistent buoyant forces driving stored CO_2 to vertically migrate through any and all breaches in the overlying caprock formation, the motivation to develop leakage pathway sealing technologies becomes especially acute.

Near the injection site, the primary driver for leakage is the over-pressurization of the pore space (Seigo et al., 2014). Farther from the injection site and throughout the storage formation once injection stops, the principal driver of CO_2 leakage is the buoyant force that results from the density difference between the CO_2 and the brine (Wang et al., 2012). At the depths considered for CO_2 injection and storage (below ~1 km) hydrostatic forces produce pressures greater than 100 bar, and thermal gradients result in temperatures greater than 50°C (van der Meer, 1993). Under these

conditions, CO_2 will exist in the supercritical state but in general it will still be less dense than the connate brines and will be subject to buoyant forces. Other characteristics will impact leakage including the permeability and chemical characteristics of the target and overlying formations, but ultimately there will be a persistent gravity force driving the CO_2 toward the surface (Nordbotten et al., 2004; Wang et al., 2012).

Sedimentary basins have distinct geothermal gradients, which will impact the leakage rate at a particular CO_2 storage site. For example, as depicted in Scenario 'a' in Figure 1, a fluid injected into the deep surface (the dark black circles indicate CO_2 reservoir conditions) will have buoyant forces acting on a rising bubble of CO_2. This force may increase as the CO_2 expands from the supercritical state (i.e., $CO_{2\,(sc)}$) to subcritical conditions (i.e., either $CO_{2\,(l)}$ or $CO_{2\,(g)}$) (Oldenburg and Lewicki, 2006; Pruess, 2008). In Scenario 'b' of Figure 1, the CO_2 would also pass through the liquid phase with complex effects on fluid properties. Note that both of these scenarios are independent of the leakage pathway (e.g., wellbore, fault, etc.). The density data included in Figure 1 illustrates the potential for nonlinear differences between the density of the brine and the CO_2 due to the complex relationship between density and phase behavior. Depending on the geothermal gradient, some parcels of CO_2 will transition from $CO_{2(sc)}$ to $CO_{2(g)}$ directly. In other regions it will pass through the liquid phase first (Oldenburg et al., 2010). In all cases, the temperature will decrease, increasing the density difference between CO_2 and brine as the fluid gets closer to the surface, effectively increasing the buoyant forces driving the CO_2 towards the surface.

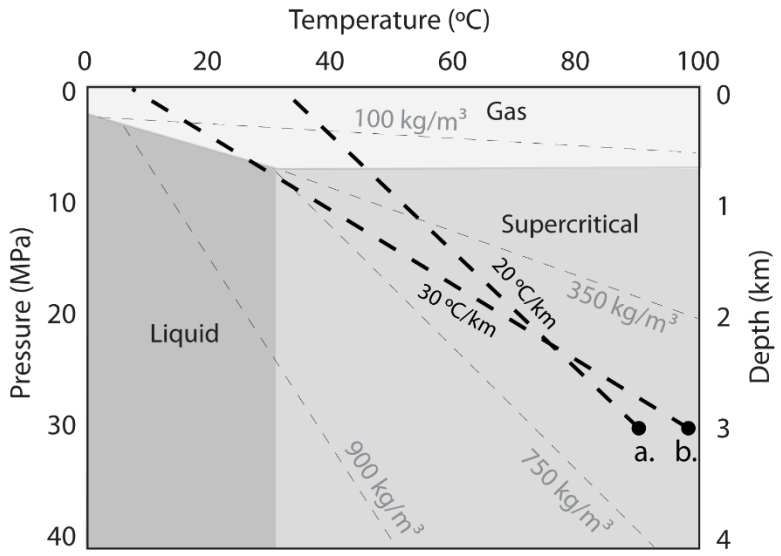

Figure 1. Site-specific geothermal gradients and the depth of the target repository will influence the buoyant driving forces that cause CO_2 to migrate toward the surface.

To manage the effects of these buoyant forces, GCS sites are selected based on the presence of an essentially impermeable caprock formation overlaying the target repository that would provide mechanical stabilization of the CO_2, preventing vertical migration while also providing time for other trapping mechanisms to further reduce the risk of vertical CO_2 migration (Kneafsey and Pruess, 2010; Widjajakusuma et al., 1999; Wollenweber et al., 2010). One of the most desirable forms of trapping is mineral trapping in which case water-soluble carbonate species react with various divalent cations (e.g., Ca, Fe, Mg), and precipitate as carbonate mineral phases (Carroll et al., 2013). Significant mineralization has the potential to reduce the porosity and permeability of the storage formation (Nogues et al., 2013). However, carbonation reactions will be limited by the low concentration of divalent cations in many perspective storage formations, including the deep saline aquifer formations that represent the largest capacity in North America (Peters, 2010). In addition, pH-sensitivity, whereby mineral carbonation occurs only once the pH rises above some critical value, will inhibit precipitation when the partial pressure of CO_2 is very high.

Consequently, carbonation reactions are not predicted to occur to any significant extent near injection wells in the near-term (Liu et al., 2011). In light of persistent buoyant forces, mitigating leakage risk near wellbores by using carbonation reactions would be an ideal mechanism to permanently trap CO_2 and block pores and fractures preventing its upward migration. However, chemical intervention would be required to regulate pH and supply divalent cations.

As stated above, the primary leakage pathways from the deep subsurface are expected to be faulty wellbores and fractures or faults that transect impermeable caprock sealing formations. A number of studies carried out over the past decade have investigated the mechanisms by which a wellbore can be compromised and transport can occur in CO_2 injection conditions. At the high pressures found in the formations relevant for geologic sequestration, the solubility of CO_2 is high enough to substantially acidify formation brines with carbonic acid (pH = ~3) (Ellis et al., 2009). The effect of these acidic brines on the cements that fill the annular spaces between the well casing and the surrounding formation is complicated and could proceed via several scenarios (Duguid and Scherer, 2010; Kutchko et al., 2008). Under the best-case scenario, the CO_2 acidified brine would only contact a small part of the bottom of the wellbore and consequently it would take hundreds of years for the cement to be degraded because of mass transfer limitations on the surface. In a related way, the corrosion products could lead to a negative feedback loop that would plug the leak and form a protective rind, as suggested by lab-scale experiments (Bai et al., 2016) as well as by examination of 30-year old well cements (Carey et al., 2010). The worst-case scenario is that the acidified brine is able to access large volumes of cement via cracks or gaps between the cement and the formation, rapidly dissolving this cement. Other studies have shown that initially small cracks can grow rapidly because of corrosion from the acidic CO_2 creating appreciable leakage

rates. Figure 2 presents a schematic of a sealed wellbore with various leakage pathways highlighted.

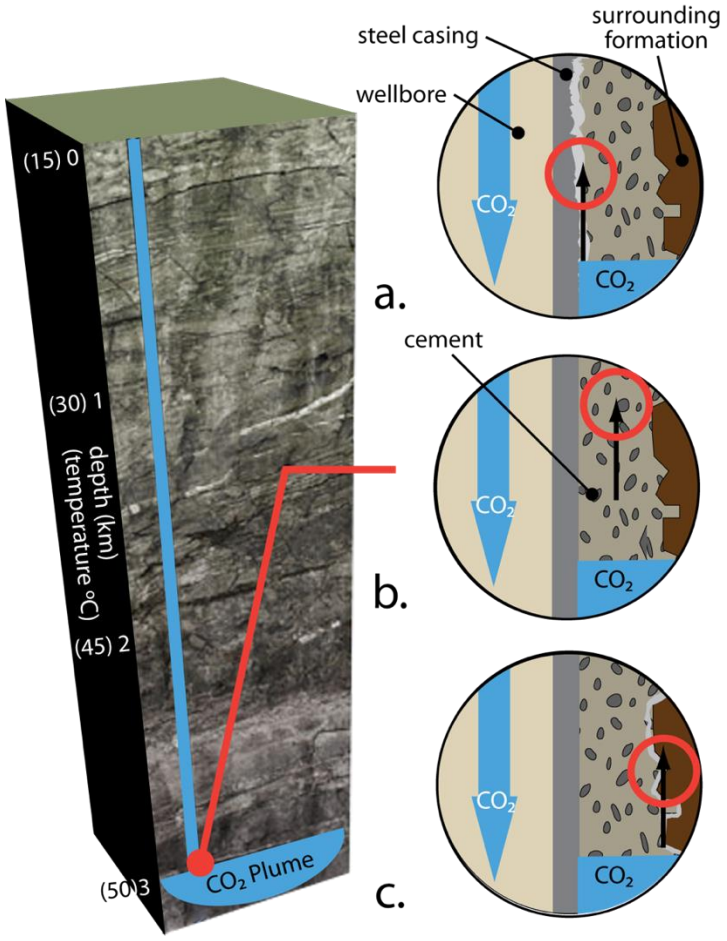

Figure 2. Schematic cross section of a plugged wellbore illustrates potential leakage pathways through: a) casing and cement; b) the cement pore space as a result of cement degradation; and c) cement and rock.

The effect of these reactions is critical to understanding wellbore stability, but the ultimate effect on formation integrity is unknown. Theoretically, one can simulate conditions that lead to degradation of wellbore integrity, and other conditions that lead to reactions that cause a caprock to self-seal (Gherardi et al., 2007). Which of these very different outcomes will occur is very

difficult to predict, and requires an improved understanding of the interrelated processes of flow and reactions in porous/fractured media.

The importance of wellbore leakage on overlying formations has come into focus recently because of the great interest in methane leakage from abandoned and non-conventional natural gas wells. Studies of abandoned wells in Pennsylvania suggest that the aggregate emissions from these wells is significant representing over 5% of total anthropogenic methane emissions in the state of Pennsylvania (Kang et al., 2015). Stable isotope analysis of shallow freshwater aquifers in the state suggest that there is naturally occurring communication between the sources of drinking water and the deep source formations for oil and gas. Also important are leaks associated with improperly completed wells and, in the case of hydraulic fracturing, so called 'ballooning' of the steel casing during the pressurization of fracturing fluid, which leads to a residual gap in the annulus between the steel casing and the cement.

Efforts to manage leaks from wellbores have focused on developing resistant cements with rheological properties that enable them to be squeezed into the gaps in the wellbore (Hovorka et al., 2006). This treatment is not often successful and can compromise the injection well. Other work has focused on engineered coatings for the cement that would lower the reactivity and protect it from corrosion (Jacquemet et al., 2012). Beyond that, comparatively little effort has been focused on developing scalable technologies that could be used to mitigate leaks if they are detected. Finding and fixing leaks in all cases can be costly and many existing strategies require detailed information about the location of a leak in order to fix it. Few technologies exist to fix leaks associated with a wellbore, limiting injection interruption and avoiding permanent well shutdown

– two of the greatest risks to an economically viable geologic CO_2 storage project (Bielicki et al., 2014). Technologies that fix leaks within the annulus between the steel casing and cement (along with compromised caprock) to solid caprock matrix are especially limited. As a result, there is an urgent need to develop technologies that would plug leakage pathways before too much CO_2 leaks through the primary caprock seal, in a passive manner that does not damage the well or injection formation, and uses chemicals that are environmentally benign.

This work presents a novel method to control the hydrologic and mechanical characteristics of subsurface pore and fractures using stimuli-responsive materials that would drive mineral carbonation reactions. In practice, the technology is based on surface-active materials that partition into the regions of the subsurface where leaks are most likely to occur and selectively clog pores and fractures within the primary caprock sealing formation. We examine aqueous fluid and additive compositions that float on super critical CO_2 and are therefore driven into leakage pathways within and around the wellbore, delivering the reactive components necessary for CO_2 to trigger calcium carbonate and silica precipitation that clogs the leakage pathway. These materials are tested using a suite of bench-scale experimental techniques and column studies. Their efficacy is validated using high-pressure column experiments and their field-scale impacts is assessed using forward modeling.

These materials could be a platform to enable smart materials with the potential to heal themselves, targeted flow control in geological formations, and tunable influence of geomechanical characteristics in subsurface repositories. At high temperature and pressure conditions, CO_2 reacts readily with Mg^{2+} or Ca^{2+} to form solids ($CaCO_{3(s)}$ or $MgCO_{3(s)}$) and these reactions have been

explored under *ex situ* conditions to sequester carbon (Gerdemann et al., 2007). This work deploys this same class of reaction in the subsurface in a targeted way that would avoid clogging and scaling within the injection zone. Low-cost, environmentally benign, coatings for mineral silicates that are sensitive to temperature and partition preferentially to the interface between CO_2 and brine are used to retard carbonation near the injection site.

The coatings provide two primary functions. The first is to impart temperature sensitivity. In the subsurface, temperature is an effective surrogate for depth and so the polymers are synthesized to collapse when temperature is below some critical value above the target formation. This collapse in the polymer coating of the mineral silicate releases the cations into solution resulting in rapid carbonation and precipitation of the solid phase and SiO_2. These precipitates seal pores and block the vertical migration of CO_2. The second function of the polymer coating is to have the particles selectively partition at the interface between the super critical CO_2 and the injected treatment aqueous slurry. This is achieved by designing the polymer chains on the surface to have an intermediate solubility in both water and CO_2. Having the mineral silicate particles partition to the interface is critical so that they exist near the leading edge of a CO_2 plume or vertical leakage event to induce precipitation once coating collapse is triggered.

2 Methods

Cation donors could be selected based on the chemistry, pressure, and temperature of the target repository to dial in the characteristics of the precipitated cements. There are a range of possible minerals that could be adopted in this application including olivine ($MgSiO_3$) and wollastonite ($CaSiO_3$). Selection would be based on geological constraints, economics, and/or life cycle environmental implications (King et al., 2010). By introducing the cation donor, this technology

could be deployed in any porous media, even those lacking an adequate cation source (Kelemen and Matter, 2008). The dissolution-precipitation chemistry will proceed spontaneously within leakage pathways and form solid carbonates and silica once reduced temperatures trigger the collapse of the polymer coating (O'connor et al., 2004). We also understand that in the context of sealing leaks in cement like those illustrated in Figure 2, it may be desirable to inject other compounds that would selectively protect the cement near the site of a leakage event such as compounds to buffer the pH of the connate brines. The general approach of developing stimuli responsive particles to tailor the chemistry in the leakage zone is the much broader outcome from this research effort.

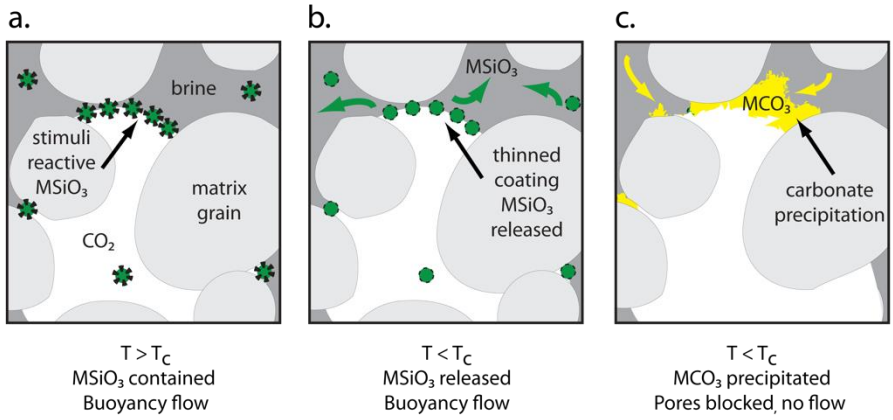

Figure 3. Schematic illustrating the leading edge of a leakage plume. The coated mineral silicates would be designed to partition at the interface between the CO_2 and brine. As the ganglion travels up through buoyant forces, the temperature will decrease (a). At some critical temperature (Tc), the block co-polymer coatings would collapse releasing the mineral silicates into solution (b). The resulting precipitation of solid carbonates would be rapid and block fluid flow (c). Note that here M = Ca or Mg or some combination of these.

Table 1. A wide range of calcium and/or magnesium silicates could be used as the reactive core for the center of reactive particles. Their suitability for use in blocking leakage is tied to their reactivity, here the reaction with CO_2 and the activation energy. Those species with a lower Ea value are more reactive.

mineral	reaction	E_a (kJ/mol)
basaltic glass	$MgSiO_3 + CO_2 = MgCO_3 + SiO_2$	80.0
olivine	$MgSiO_4 + 2CO_2 = 2MgCO_3 + 2SiO_2$	76.2
serpentine	$Mg_3Si_2O_5(OH)_4 + 3CO_2 = 3MgCO_3 + 2SiO_2 + 2H_2O$	70.1
albite	$2NaAlSi_2O_8 + CO_2 = Na_2CO_3 + 6SiO_2 + Al_2O_3$	65.0
wollastonite	$CaSiO_3 + CO_2 = CaCO_3 + SiO_2$	54.7
talc	$Mg_3Si_4O_{10}(OH)_2 + 3CO_2 = 3MgCO_3 + 4SiO_2 + H_2O$	51.4
anorthite	$CaAl_2Si_2O_8 + CO_2 = CaCO_3 + 2SiO_2 + Al_2O_3$	48.4

Recent work by Lee et al., Ma et al., and others has shown that stimuli responsive coatings can be created by mimicking the properties of muscle linkage proteins (Lee et al., 2007; Ma et al., 2013). The approach is easy, inexpensive, and safe to apply, and it has already been applied in a variety of applications including drug delivery and slow release fertilizers. Efforts to develop temperature-responsive polymers are generally based on the deposition of a polydopamine (Pdop) layer on a salty substrate using spontaneous self-polymerization in weak alkaline solution. Once the Pdop layer is attached to the substrate, an application-specific stimuli-responsive compound can be attached to the Pdop layer. Surface-initiated atom transfer radical polymerization (SI-ATRP) is the process used to bind responsive moieties to the Pdop-based initiator. Ma et al. developed temperature responsive fertilizers using a "polydopamine-g-polymer brush" structure with a grafted stimuli-sensitive polymer brush corona. Figure 3 provides a schematic of the synthesis of these coatings. It involves three steps. In the first, the dopamine polymerization produces a coating on the salty core. In the second step, the particles are treated with an initiator for the polymerization reaction in Figure 4 using 2-bromoisobutyryl bromide (BIBB)). In the last step, N-

Isopropylacrylamide is polymerized on the surface of the particles to create the temperature sensitive brushes.

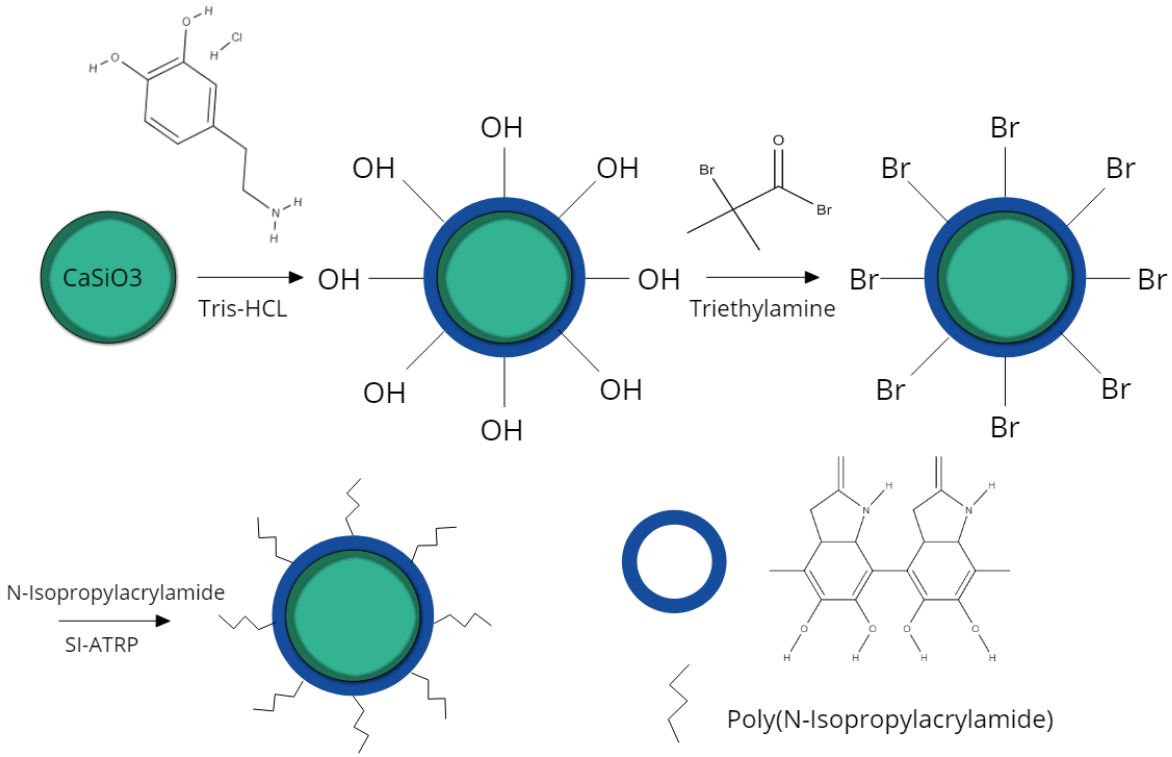

Figure 4. Functionalization of a cation donor (wollastonite or olivine, indicated in this figure in green) would be carried out using a polydopamine (blue layer here) coating. This coating would then be functionalized (here using BIBB) to initiate polymerization, here using N-Isopropylacrylamide to create temperature-sensitive brushes. Above a critical temperature, these brushes are collapsed inhibiting the release of the material in the soluble core. Below a certain temperature, the brushes become extended prompting the release of the salty soluble core into the surrounding water phase. (Adapted from (Ma et al., 2013))

In the Ma et al. work, the reacted particles are designed to become soluble below a so-called lower critical solution temperature (LCST) of 32 ºC. At temperatures above this, the polymer brushes

are in a collapsed state, which makes the water permeability of the multilayered coating low, limiting release of the soluble core. When the temperature drops below 32 ºC, the thermosensitive chains become soluble and expand to become channels for water that favor release of the material in the core. In practice, a LCST of 32ºC would correspond to a depth of 1-2 km below the surface depending on the site.

2.1 Particle Coating Procedure

Here, we have adapted a polymer-coating procedure from Yu et al., in which we grafted a Poly(N,N-dimethylaminoethyl methacrylate) (PDMAEMA) polymer, with a LCST of approximately 45-50 ºC, on calcium silicate particles ($CaSiO_3$, Sigma-Aldrich, 99%, average powder diameter = 10.2 μm, SD = 8.4 μm, spongy/aggregated shape). We closely followed the coating procedures outlined in their work, with the exception of using $CaSiO_3$ particles rather than hollow mesoporous silica nanoparticles. Figure 5 shows the $CaSiO_3$ particles, both uncoated and coated, that were used here.

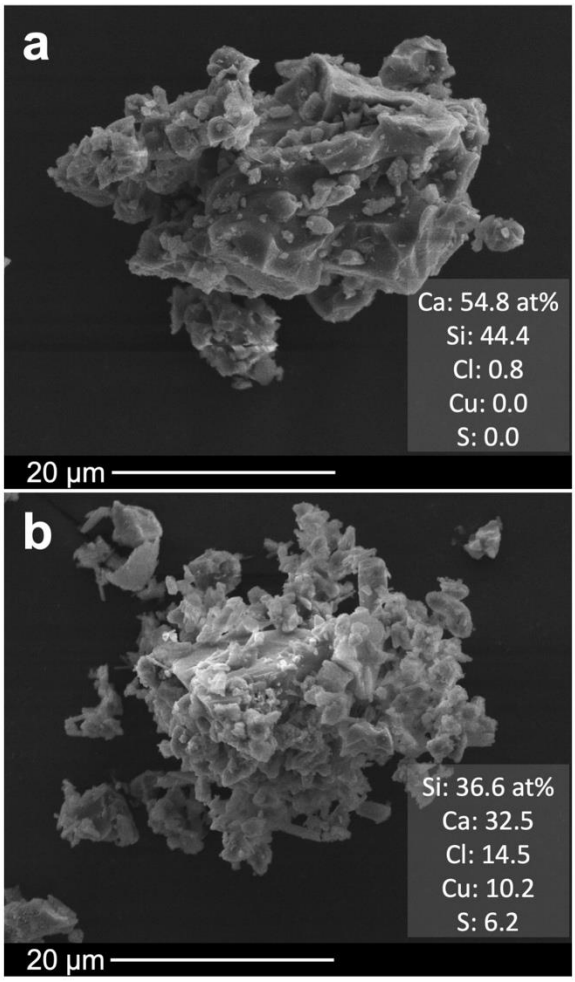

Figure 5. SEM images of (a) an uncoated $CaSiO_3$ particle used in this work, with EDS indicating predominantly Ca and Si (O excluded) and (b) a polymer-coated $CaSiO_3$ particle that shows the presence of Cl, Cu, and S from the coating.

2.2 Sand Column Experiments

Sand columns, 1.59 cm in diameter and nominally 2 cm in length, were prepared in a similar manner to our previous work (Plattenberger et al., 2019, 2018) by loading 316 stainless-steel columns with washed sand and capping each end with washers and stainless-steel mesh. The air permeability of each column was measured and subsequently, either polymer-coated or uncoated

$CaSiO_3$ particles were suspended in deionized water (3g/L) and injected into the columns at pressures increasing from 0.5 MPa to 10 MPa during the injection process. A 20 μm porous disc was placed at the outlet end of the columns during injection to retain the powders. After injection, the columns were dried at 75 ºC and permeability was again measured. The outlet end of each column was sealed with a Teflon cap and the columns were reacted in CO_2-saturated water in a stirred stainless-steel vessel at either 35 ºC or 70 ºC (below and above the LCST, respectively) with a headspace pressure of 3.4 MPa. The water was buffered with 0.1 M NaOH to isolate the effect of temperature on reactivity of coated vs. uncoated particles and limit the impact of low pH, caused by dissolved carbonate, which may confound the effects of temperature. The 70 ºC columns were reacted for 96 hrs and, to account for chemical kinetics, the 35 ºC columns were reacted for 475 hr. After the reaction periods, the columns were again dried at 75 ºC and the air permeability was measured. Our previous work has established that oven drying has no discernable impact on the permeability compared to similar air-dried columns. The columns were subsequently injected with epoxy (Buehler EpoThin 2) and sectioned lengthwise with a diamond cutoff saw for SEM-EDS observation and mapping (FEI Quanta LV200).

2.3 Modeling Particle Transport

For the mineral silicate particles to be effective in sealing leakage sites, it is important that they are transported throughout the subsurface at high enough concentrations to block flow after reaction. The transport of the particles after injection can be predicted using the advection-dispersion equation in conjunction with colloidal filtration theory (Tian et al., 2010). The general form of this equation is given in Equation 1:

$$\frac{\delta C}{\delta t} = D\frac{\delta^2 C}{\delta x^2} - v\frac{\delta C}{\delta x} - k_a C \qquad \text{Equation (1)}$$

where C is particle concentration, D is the dispersion coefficient of the particles in the fluid, v is the advection velocity, and k_a is the rate of particle retention. The particle retention rate was determined using the single-contact collector efficiency (Tufenkji and Elimelech, 2004) and is a function of the Peclet Number, Aspect Ratio, van der Waals Number, Gravitational Number, and alpha parameter. Alpha is dependent on particle surface properties and fluid ionic strength and signifies the likelihood of attachment to a collector site given a collision. For this model, flow conditions were assumed to be steady-state, so particle re-mobilization can be taken as zero (Tian et al., 2010).

Particle transport was simulated using a Python-wrapped partial differential equations solver called FEniCS (Langtangen and Logg, 2016). This package uses the finite-element method to solve Equation 1 for a number of points in a predetermined flow field. In this simulation, fluid is injected at a point source with a fixed initial particle concentration and constant flow rate. The fluid spreads radially through a porous medium and particle concentration is calculated as a function of time and distance from the source. Pore blocking by filtered particles is accounted for by decreasing the porosity of the modeled medium based on the decrease in concentration at each time step.

Table 2. Variables used in particle transport model simulations.

Parameter	Units	Symbol	Low	High	Nominal Value	Source
Dispersion Coefficient	m^2/s	D	7.40E-12	7.40E-11	3.60E-11	(Pinheiro et al., 2007)
Flow Rate	m^3/s	Q	0.01	0.1	0.014	(Nordbotten et al., 2005)
Porosity	-	n	0.25	0.4	0.33	(Manger, 1963)
Inflow Concentration	g/L	c_i	0.03	3	1	Design Parameter
Particle Diameter	μm	d_p	0.1	75	8	Design Parameter
Grain Size	μm	d_c	50	250	100	(Wardlaw and Cassan, 1979)
Hamaker Constant	J	A	3.00E-21	8.00E-20	5.00E-20	(Tufenkji and Elimelech, 2004)
Viscosity	Pa-s	μ	1.00E-05	1.00E-04	5.00E-05	(Heidaryan et al., 2011)
Temperature	K	T	298	373	325	Design Parameter
Fluid Density	g/cm^3	ρ_f	0.19	1	0.5	Engineering Toolbox
Alpha	-	α	0.002	0.1	0.018	(Rahman et al., 2013)

Simulations were conducted for a range of conditions that can be expected for an injection into a deep sandstone formation (Table 2). A sensitivity analysis was done for each parameter by simulating high and low values for each variable against the nominal value for all other variables. For this analysis, a 20-day pumping period was simulated, resulting in a plume filling a 50 meter radius to a thickness of 10 meters. A long-term simulation was also conducted to examine the deposition of particles in pore spaces. Here, we set the simulation for 5 years of pumping with the nominal value parameters, with the exception of particle size. To facilitate longer particle transport distances, particle diameter was set to 1.0 μm.

3 Results

A combination of laboratory experiments and simulations were performed to demonstrate that this approach could be used in principal to mitigate some of the leakage risk associated with CO_2

injection. Laboratory experiments for both coated and uncoated particles at temperatures above and below the polymer activation temperature were used to demonstrate that these polymer coatings could be used under reservoir conditions to target reactivity. Particle transport modeling simulations were used to understand the particle design and delivery conditions that would be best suited for deploying these particles in the field.

3.1 Experimental Results

The impacts on sand column permeability of reaction periods above and below the LCST are illustrated in Figure 6. The injected but unreacted columns show a relatively uniform distribution of $CaSiO_3$ throughout the pore space (as evidenced by cross-section SEM micrographs and their corresponding Ca EDS maps in Figure 6a), with few voids filled with epoxy. Figure 6b represents the scenario in which uncoated particles are injected into a well, where they would be exposed to relatively high temperatures, referenced in Figure 6 in the presence of dissolved CO_2. Here, the $CaSiO_3$ particles react to produce primarily $CaCO_3$, shown as darker red clusters, as well as $amSiO_2$. In 96 hours of reaction, the permeability of two columns at 70 C decreased by 1.20 and 1.25 orders of magnitude while the mass of the particles increased by 23.31 and 21.61%. Contrasting those columns with ones injected with coated $CaSiO_3$, Figure 6c, there appeared to be significantly fewer and smaller Ca clusters, which we speculate has a direct impact on permeability. In those two columns, permeability decreased by only 0.62 and 0.58 orders of magnitude and mass increased 15.37 and 14.25%, both of which are considerably smaller changes than the uncoated columns.

Figure 6d is illustrative of $CaSiO_3$ particles that migrate up along a wellbore or through faults in caprock where temperatures would decrease relative to those deeper in the formation. Because the reaction period was extended to account for chemical kinetics, there appears to be a similar distribution of $CaCO_3$ clusters at 35 ºC in this scenario compared to the uncoated 70 C scenario. During the reaction period, the permeability of these columns decreased by 0.90 and 0.81 orders of magnitude and the mass increased by 19.67 and 18.39%.

As the temperature decreases lower than the LCST (approximately 45-50 ºC for the particular polymer chosen for this work), the polymers are expected to extend, allowing $CaSiO_3$ dissolution and reaction with dissolved CO_2. In that scenario, Figure 6e, the reaction appeared to have a similar effect on permeability and $CaCO_3$ precipitation as the uncoated 35 ºC scenario. The permeability decreased 0.74 and 0.72 orders of magnitude and the masses increased by 16.65 and 16.56%. It is important to reiterate that the kinetics of silicate carbonation slow down considerably at lower temperatures (as shown when comparing the difference in permeability between 6B and 6D). So even though the reactivity of the coated particles goes up only modestly between 6C and 6D, the polymer is performing as it should. The principal value of the polymer is that it is limiting permeability drop within the target formation where the temperature remains high (comparing 6B and 6C).

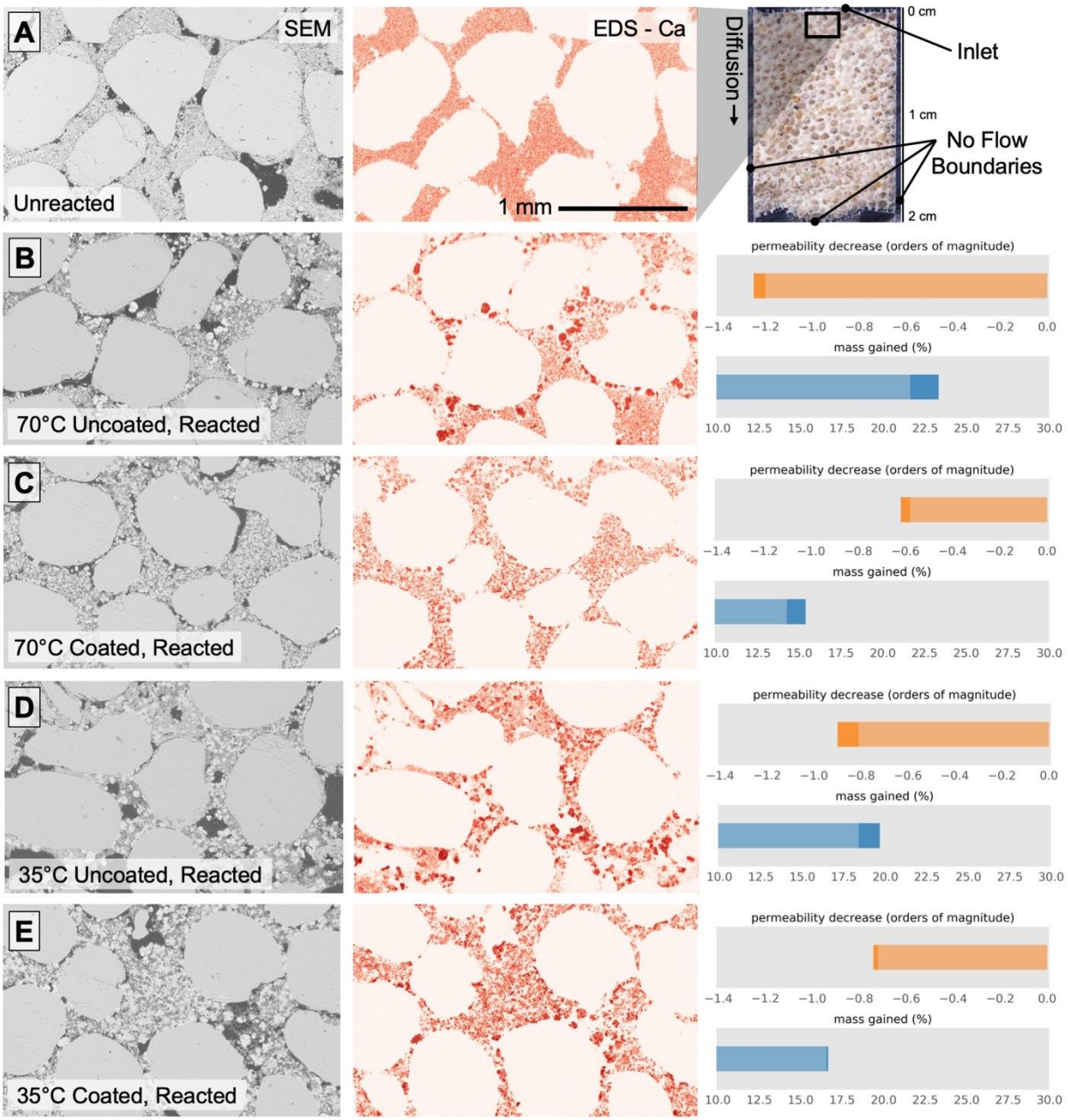

Figure 6. (a) A representative backscattered SEM micrograph alongside the corresponding Ca EDS map of the inlet of a $CaSiO_3$ injected but unreacted sand column shows a relatively uniform distribution of Ca in the pore space. (b) When uncoated $CaSiO_3$ is reacted at 70 C, large clusters of $CaCO_3$ appear in the EDS map compared to (c) when coated $CaSiO_3$ particles are used. Below

the LCST, at 35 ºC, (d) uncoated and (e) coated Ca maps appear relatively similar, compared to the higher temperature columns above the LCST in (a) and (b).

3.2 Modeling Results

The simulations produced a range of particle transport conditions, ranging from scenarios with almost no particle deposition (particles suspended throughout entire plume) to scenarios where nearly all particles were deposited in pore spaces within a few meters of the inflow. To limit leakage risk in geologic carbon storage conditions, it is desirable to maintain a balance between transport and deposition. The particles must be mobile enough to move with the CO_2 plume, but filtered at a rate that allows them to build up in pore spaces near leakage sites. To design particle properties and delivery techniques that support these goals, a range of simulations were conducted and the results are presented in Figure 7. These plots depict particle concentrations in the CO_2 plume (normalized to the injection concentration) as a function of distance from the injection site. The results are grouped based on whether they are related to particle properties (e.g., diameter, coating), injection characteristics (e.g., flow rate, concentration), or rock formation properties (permeability, temperature, etc.), to provide initial insight into which properties matter the most in injected particle transport.

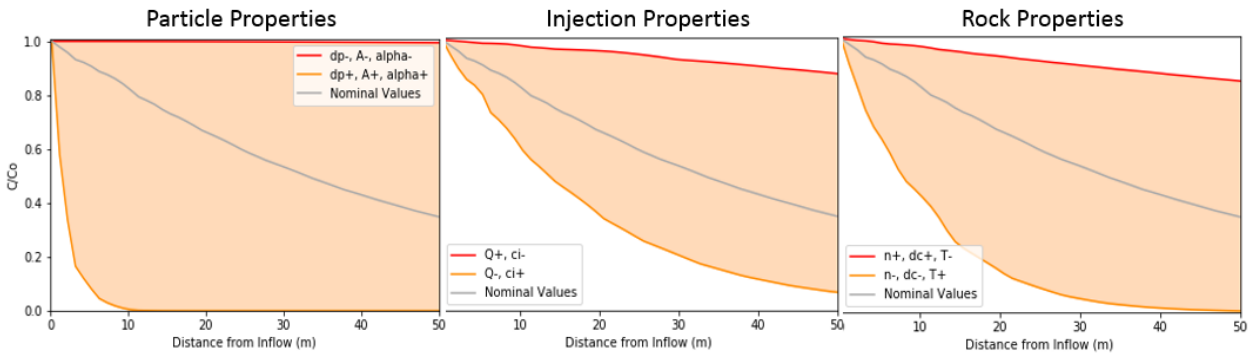

Figure 7. Line plots showing the fraction of particles remaining suspended in the CO2 plume as a function of distance from the inflow. The upper (dark orange) and lower (light orange) bounds signify the extreme effects of each group of parameters on transport, while the central line (grey) is the result of the simulation with nominal values. The shaded area represents the range of possible transport conditions changing only the given variables.

It is apparent that the effects of particle size and coating (contributing to alpha and the Hamaker constant) on particle transport are significant, especially when compared to properties pertaining to fluid and rock conditions. This suggests that transport behavior can be controlled by tailoring the silicate nanoparticles based on the conditions of the injection site. The results of the sensitivity analysis using a 20-day pumping simulation are shown in Figure 8. Effects of realistic high and low values for each parameter were tested against nominal values, showing the effects of each individual parameter on particle transport behavior.

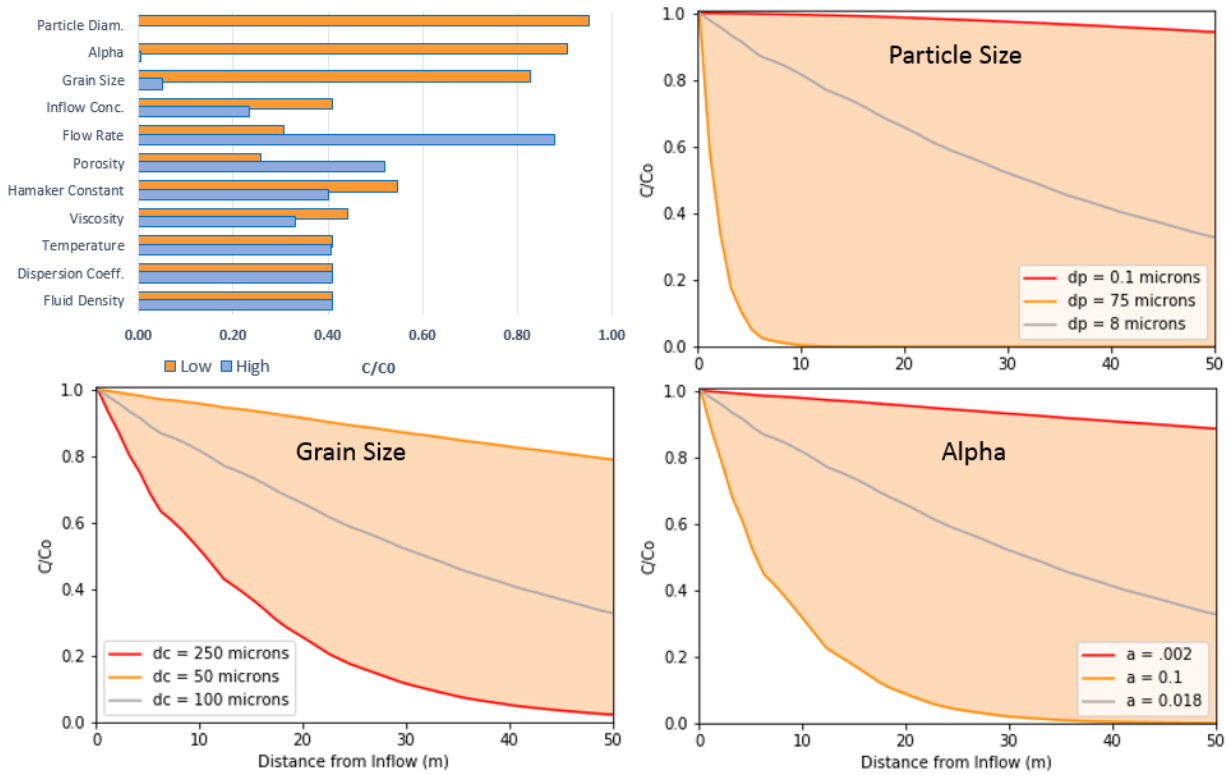

Figure 8. Sensitivity analysis showing the effects of each input parameter on particle concentration at the leading edge of the CO_2 plume. Concentration is given as a fraction of the inflow concentration. Line plots show the effects of the three most impactful variables on particle transport as a function of distance with high, low, and nominal values.

This analysis reveals that the silicate particle size, coating properties (alpha), and rock formation grain size (pore size) have the largest impact on the transport distance of the particles. The 75 micron-diameter particles were removed completely from the plume within 10 meters of the inflow, while 0.1 micron particles retained above 90% of the inflow concentration in the entire plume. Similar trends are seen with alpha and grain size. High alpha values resulted in complete particle deposition within 50 meters of the inflow, while low values retained 90% of the inflow concentration. Grain size, porosity and flow rate also have significant impacts on particle transport,

providing ranges of 75%, 60%, and 30% differences in plume edge concentrations after 20 days, respectively. It is worth noting that at these injection concentrations, blocking of pores near the injection site was not a cause of major permeability loss. However, at concentrations much higher than 5-10 g/L, pore clogging near the inflow begins to become a significant factor affecting particle transport. Additionally, the actual value for alpha may be lower than suggested by the nominal estimate because of its dependence on ionic strength (Rahman et al., 2013). Because the fluid is supercritical CO_2, there is not an appreciable ionic strength and the particles will be less likely to adhere to grain surfaces. This means that particle size is the easiest variable to manipulate for the alteration of transport behavior.

To determine long-term particle deposition rates throughout the plume, a 5-year simulation was run using nominal values except for injected particle diameters of 1.0 micron. The CO_2 was injected into a sandstone formation at a concentration of 5.0 g/L, forming a plume with a thickness of 10 meters. Relatively small particles were selected to allow for further transport and more even deposition into the formation pore spaces with a higher inflow concentration. Figure 9 shows the volume of pore space occupied by the silicate particles as a function of distance from the injection site. This simulation resulted in a fairly even distribution of particles after 5 years, ranging from 2.10% of the pore volume near the inflow to 0.25% of the pore volume around 200 meters. As simulation time progressed, pores become increasingly populated with particles filtered from the fluid, especially near the injection well. In full-scale geologic storage sites, particle volumes in pore spaces should increase indefinitely with pumping time.

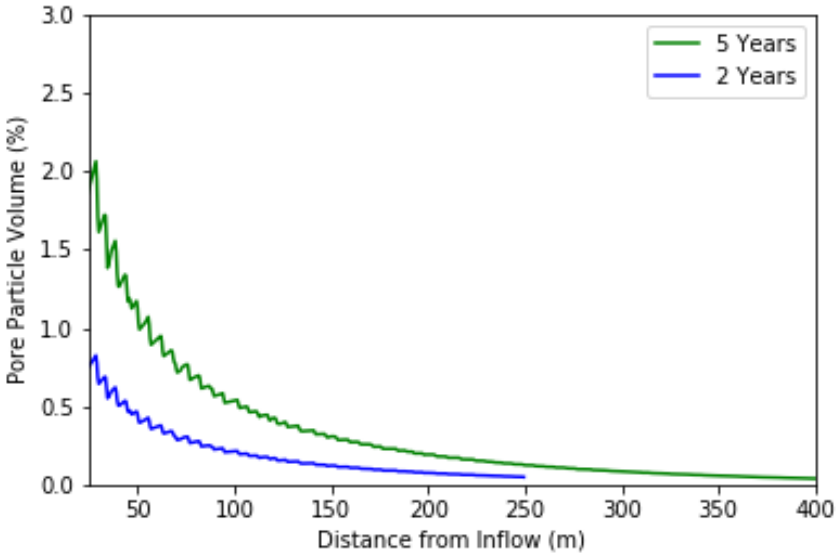

Figure 9. Pore volume filled by particles as a function of distance from inflow. As pumping continues, silicates build up in the pore spaces of the formation, as shown by the difference in the 2- and 5-year time scales.

Laboratory experiments show that permeability in the injection medium is effectively reduced when silicate volume is 47% of the total pore volume (Plattenberger et al., 2019). It should be noted, however, that this is a single observation point and not a lower bound. Injecting particles at concentrations anywhere near this level is not feasible. Instead, we rely on the deposition of particles over time. By adjusting particle size and inflow concentrations, it is possible to alter the level of deposition throughout the plume. Larger particles and higher inflow concentrations will cause more rapid deposition near the inflow (useful for short pumping periods), while small particles at lower concentrations will tend to be distributed more evenly throughout the entire plume (longer pumping periods). Particles are also likely to selectively fill leakage areas because of the activation of the polymer coating, which allows for dissolution and carbonation of the

mineral silicates. This effectively removes particles from the plume and deposits them where CO_2 is escaping upwards.

While useful for predicting two-dimensional particle transport behavior, this modeling is limited in its scope. We assume a plume of uniform thickness, whereas CO_2 plumes tend to thin as they spread radially from the inflow site (Nordbotten et al., 2005). In addition, the effects of gravity on the upward migration of the particles is only accounted for in the determination of the particle filtration rate.

3.3 Nanoparticle design

The results of the modeling and provide insight into how one might begin to design nanoparticles to be used in this manner. Varying the particle size and shape is the most effective and easy to control means of tailoring transport to a particular target formation. For the sandstone formation and supercritical CO_2 fluid simulated here, particle sizes ranging from 1 to 8 microns in diameter are most effective for creating an even distribution throughout the plume. With formations of high porosity and/or large grain sizes, relatively larger particles are appropriate because transport is more effectively facilitated. For long pumping periods, low flow rates, or high inflow concentrations, relatively smaller particles should be used to maintain even distribution throughout the plume and avoid pore clogging at the injection site. The second most effective way to control transport is by varying the chemistry of the functional coatings on the outside of the nanoparticle because this will directly influence the likelihood that a particle will adhere to the wall of a pore. With additional validation, the modeling tool developed here could be used to estimate appropriate particle diameters for real-world injection sites.

While particle buoyancy due to surface properties was not simulated in this model, Figure 10 illustrates the possibility of using nanoporous silicates to change the buoyancy of particles in the fluid. The nanoparticles shown in Figure 10 were synthesized in our lab and could be filled with polymers or other material to ensure that they 'float' in $scCO_2$ and maintain a high concentration at the upper edge of the plume. The literature also suggests that particle shape will affect the alpha parameter, with round particles being less likely to adhere to grain surfaces (lower alpha value).

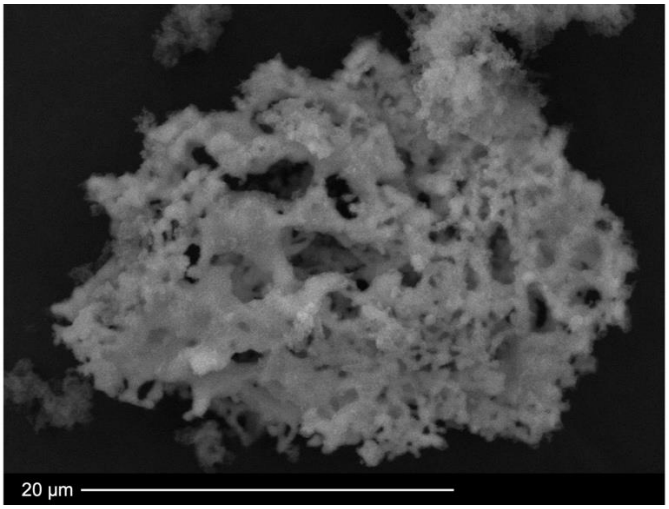

Figure 10. Many of the physical characteristics of the injected particles may be tuned to meet the demands of a reservoir. Here we present an SEM image of a $CaSiO_3$ particle synthesized in our lab using the citrate-nitrate gel combustion method proposed by (Huang and Chang, 2009). Such particles would have much greater likelihood of moving toward the regions of the target formation where leakage is expected.

4 Conclusions

The results reported here suggest that it would be possible to use targeted precipitation of coated mineral silicate nanoparticles to improve the security of geologic carbon sequestration. Existing and proposed injection sites are vulnerable to buoyancy-driven release of CO_2 near well casings

and through cracks in the caprock formation. The addition of mineral silicate particles to the injected fluid facilitates the sealing of rock and cement via carbonation reactions. The use of a poly(N,N-dimethylaminoethyl methacrylate) polymer coating on the silicate particles allows them to be functionalized at a desired temperature, in this case, 45-50℃, corresponding to a specific depth within the injection formation above which you would not want CO_2 to travel.

Experiments showed that these mineral silicates are effective in reducing permeability in sand columns. Permeability reductions ranging from 0.6 to 1.2 orders of magnitude were achieved, depending on the temperature and presence of polymer coating. Our experiments showed that the coated particles decreased permeability more intensely below the desired activation temperature than above it. This signifies targeted dissolution of the mineral silicates based on temperature, allowing them to selectively plug upward leaks as the fluid cools while moving laterally with the CO_2 plume.

Modeling of nanoparticle injection processes allowed us to consider the engineering design and delivery of these nanoparticles that might be desired for most efficient use in practice. A 2D modeling domain was defined and nanoparticle transport into an idealized formation was estimated. The results suggest that a number of design parameters related to the particle design, injection conditions and target formation geology impact particle penetration into the formation. The size and surface properties of the nanoparticles have the greatest effect on transport distance, followed closely by the grain size of the porous medium.

Taken together, the experimental and modeling work reported here suggest ways in which this concept might be translated into practice. Buoyancy of the nanoparticles is an important consideration given that many of the leakage pathways will occur in the caprock and so it would be important to ensure that most of the nanoparticles travel naturally toward the top of the formation. But given how many different silicates could be used, how tailorable their characteristics are, and how quickly the field of functionalized coatings is growing, these results suggest that this approach could be an important enabling technology for limiting the risk associated with geologic carbon storage.

5 References

Bai, M., Zhang, Z., Fu, X., 2016. A review on well integrity issues for CO2 geological storage and enhanced gas recovery. Renew. Sustain. Energy Rev. https://doi.org/10.1016/j.rser.2016.01.043

Bielicki, J.M., Pollak, M.F., Fitts, J.P., Peters, C.A., Wilson, E.J., 2014. Causes and Financial Consequences of Geologic CO2 Storage Reservoir Leakage and Interference with other Subsurface Resources. Int. J. Greenh. Gas Control 20, 272–284.

Bohnhoff, M., Zoback, M.D., 2010. Oscillation of fluid-filled cracks triggered by degassing of CO2 due to leakage along wellbores. J. Geophys. Res. 115, B11305.

Bruant, R.G.J., Celia, M.A., Guswa, A.J., Peters, C.A., 2002. Safe Storage of CO2 in Deep Saline Aquifiers. Environ. Sci. Technol. 36, 240A–245A. https://doi.org/10.1021/es0223325

Carey, J.W., Svec, R., Grigg, R., Zhang, J., Crow, W., 2010. Experimental investigation of

wellbore integrity and CO< sub> 2</sub>–brine flow along the casing–cement microannulus. Int. J. Greenh. Gas Control 4, 272–282.

Carroll, S.A., McNab, W.W., Dai, Z., Torres, S.C., 2013. Reactivity of Mount Simon Sandstone and the Eau Claire Shale Under CO2 Storage Conditions. Environ. Sci. Technol. 47, 252–261. https://doi.org/10.1021/es301269k

Duguid, A., Scherer, G.W., 2010. Degradation of oilwell cement due to exposure to carbonated brine. Int. J. Greenh. Gas Control 4, 546–560.

Ellis, B.R., Crandell, L.E., Peters, C.A., 2009. Limitations for brine acidification due to SO2 co-injection in geologic carbon sequestration. Int. J. Greenh. Gas Control 4, 575–582.

Gerdemann, S.J., O'Connor, W.K., Dahlin, D.C., Penner, L.R., Rush, H., 2007. Ex situ aqueous mineral carbonation. Environ. Sci. Technol. 41, 2587–2593.

Gherardi, F., Xu, T., Pruess, K., 2007. Numerical modeling of self-limiting and self-enhancing caprock alteration induced by CO2 storage in a depleted gas reservoir. Chem. Geol. 244, 103–129.

Heidaryan, E., Hatami, T., Rahimi, M., Moghadasi, J., 2011. Viscosity of pure carbon dioxide at supercritical region: Measurement and correlation approach. J. Supercrit. Fluids. https://doi.org/10.1016/j.supflu.2010.12.006

Hovorka, S.D., Benson, S.M., Doughty, C., Freifeld, B.M., Sakurai, S., Daley, T.M., Kharaka, Y.K., Holtz, M.H., Trautz, R.C., Nance, H.S., 2006. Measuring permanence of CO2 storage

in saline formations: the Frio experiment. Environ. Geosci. 13, 105–121.

Huang, X.-H., Chang, J., 2009. Synthesis of nanocrystalline wollastonite powders by citrate–nitrate gel combustion method. Mater. Chem. Phys. 115, 1–4.

IPCC, 2014. Mitigation of Climate Change. Contribution of Working Group III to the Fifth Assessment Report of the Intergovernmental Panel on Climate Change. Cambridge Univ. Press. Cambridge, UK New York, NY.

Jacquemet, N., Pironon, J., Lagneau, V., Saint-Marc, J., 2012. Armouring of well cement in H 2 S–CO 2 saturated brine by calcite coating–Experiments and numerical modelling. Appl. Geochemistry 27, 782–795.

Kang, M., Baik, E., Miller, A.R., Bandilla, K.W., Celia, M.A., 2015. Effective permeabilities of abandoned oil and gas wells: Analysis of data from Pennsylvania. Environ. Sci. Technol. 49, 4757–4764. https://doi.org/10.1021/acs.est.5b00132

Kelemen, P.B., Matter, J., 2008. In situ carbonation of peridotite for CO2 storage. Proc. Natl. Acad. Sci. 105, 17295–17300.

King, H.E., Plümper, O., Putnis, A., 2010. Effect of Secondary Phase Formation on the Carbonation of Olivine. Environ. Sci. Technol. 44, 6503–6509. https://doi.org/10.1021/es9038193

Kneafsey, T.J., Pruess, K., 2010. Laboratory flow experiments for visualizing carbon dioxide-induced, density-driven brine convection. Transp. Porous Media 82, 123–139.

Kutchko, B.G., Strazisar, B.R., Lowry, G. V, Dzombak, D.A., Thaulow, N., 2008. Rate of CO2 Attack on Hydrated Class H Well Cement under Geologic Sequestration Conditions. Environ. Sci. Technol. 42, 6237–6242.

Langtangen, H.P., Logg, A., 2016. Solving PDEs in Minutes - The FEniCS Tutorial Volume I. Manual. https://doi.org/10.1007/978-3-319-52462-7

Lee, H., Dellatore, S.M., Miller, W.M., Messersmith, P.B., 2007. Mussel-inspired surface chemistry for multifunctional coatings. Science (80-.). 318, 426–430.

Liu, F., Lu, P., Zhu, C., Xiao, Y., 2011. Coupled reactive flow and transport modeling of CO2 sequestration in the Mt. Simon sandstone formation, Midwest U.S.A. Int. J. Greenh. Gas Control 5, 294–307. https://doi.org/http://dx.doi.org/10.1016/j.ijggc.2010.08.008

Ma, Z., Jia, X., Hu, J., Liu, Z., Wang, H., Zhou, F., 2013. Mussel-Inspired Thermosensitive Polydopamine-graft-Poly(N-isopropylacrylamide) Coating for Controlled-Release Fertilizer. J. Agric. Food Chem. 61, 12232–12237. https://doi.org/10.1021/jf4038826

Manger, E.G., 1963. Porosity and Bulk Density of Sedimentary Rocks, Porosity and Bulk Density of Sedimentary Rocks.

Nogues, J.P., Fitts, J.P., Celia, M.A., Peters, C.A., 2013. Permeability evolution due to dissolution and precipitation of carbonates using reactive transport modeling in pore networks. Water Resour. Res. 49, 6006–6021.

Nordbotten, J.M., Celia, M.A., Bachu, S., 2005. Injection and storage of CO2 in deep saline

aquifers: Analytical solution for CO2 plume evolution during injection. Transp. Porous Media 58, 339–360. https://doi.org/10.1007/s11242-004-0670-9

Nordbotten, J.M., Celia, M.A., Bachu, S., Dahle, H.K., 2004. Semianalytical solution for CO2 leakage through an abandoned well. Environ. Sci. Technol. 39, 602–611.

O'connor, W.K., Dahlin, D.C., Rush, G.E., Gerdemann, S.J., Penner, L.R., Nilsen, D.N., 2004. Aqueous mineral carbonation: Mineral availability, pretreatment, reaction parametrics, and process studies. US DOE, DOE/ARC-TR-04-002.

Oldenburg, C.M., Lewicki, J., Pan, L., Dobeck, L., Spangler, L., 2010. Origin of the patchy emission pattern at the ZERT CO2 release test. Environ. Earth Sci. 60, 241–250.

Oldenburg, C.M., Lewicki, J.L., 2006. On leakage and seepage of CO2 from geologic storage sites into surface water. Environ. Geol. 50, 691–705.

Peters, C.A., 2010. Basin-scale leakage risks from geologic carbon sequestration: Impact on carbon capture and storage energy market competitiveness.

Pinheiro, J.P., Domingos, R., Lopez, R., Brayner, R., Fiévet, F., Wilkinson, K., 2007. Determination of diffusion coefficients of nanoparticles and humic substances using scanning stripping chronopotentiometry (SSCP). Colloids Surfaces A Physicochem. Eng. Asp. https://doi.org/10.1016/j.colsurfa.2006.08.054

Plattenberger, D.A., Ling, F.T., Peters, C.A., Clarens, A.F., 2019. Targeted Permeability Control in the Subsurface Via Calcium Silicate Carbonation. Environ. Sci. Technol. In Review.

Plattenberger, D.A., Ling, F.T., Tao, Z., Peters, C.A., Clarens, A.F., 2018. Calcium Silicate Crystal Structure Impacts Reactivity with CO2 and Precipitate Chemistry. Environ. Sci. Technol. Lett. 5, 558–563. https://doi.org/10.1021/acs.estlett.8b00386

Pruess, K., 2008. Leakage of CO2 from geologic storage: Role of secondary accumulation at shallow depth. Int. J. Greenh. Gas Control 2, 37–46.

Rahman, T., George, J., Shipley, H.J., 2013. Transport of aluminum oxide nanoparticles in saturated sand: Effects of ionic strength, flow rate, and nanoparticle concentration. Sci. Total Environ. https://doi.org/10.1016/j.scitotenv.2013.06.049

Seigo, S.L., Arvai, J., Dohle, S., Siegrist, M., 2014. Predictors of risk and benefit perception of carbon capture and storage (CCS) in regions with different stages of deployment. Int. J. Greenh. Gas Control 25, 23–32.

Tian, Y., Gao, B., Silvera-Batista, C., Ziegler, K.J., 2010. Transport of engineered nanoparticles in saturated porous media. J. Nanoparticle Res. https://doi.org/10.1007/s11051-010-9912-7

Tufenkji, N., Elimelech, M., 2004. Correlation Equation for Predicting Single-Collector Efficiency in Physicochemical Filtration in Saturated Porous Media. Environ. Sci. Technol. https://doi.org/10.1021/es034049r

van der Meer, L.G.H., 1993. The conditions limiting CO2 storage in aquifers. Energy Convers. Manag. 34, 959–966.

Wang, S., Edwards, I.M., Clarens, A.F., 2012. Wettability phenomena at the co2–brine–mineral

interface: Implications for geologic carbon sequestration. Environ. Sci. Technol. 47, 234–241.

Wardlaw, N.C., Cassan, J.P., 1979. Oil recovery efficiency and the rock-pore properties of some sandstone reservoirs. Bull. Can. Pet. Geol. 27, 117–138.

Widjajakusuma, J., Biswal, B., Hilfer, R., 1999. Quantitative prediction of effective material properties of heterogeneous media. Comput. Mater. Sci. 16, 70–75. https://doi.org/10.1016/s0927-0256(99)00047-6

Wollenweber, J., Alles, S., Busch, A., Krooss, B.M., Stanjek, H., Littke, R., 2010. Experimental investigation of the CO2 sealing efficiency of caprocks. Int. J. Greenh. Gas Control 4, 231–241.

Appendix A – Transport Modeling Script

```
#Tyler Brown 2019 - Department of Engineering Systems and the Environment
#University of Virginia Advanced Research Computing Lab

# FEniCS Project
# @book{LangtangenLogg2017,
#  title = {Solving PDEs in Python},
#  author = {Hans Petter Langtangen and Anders Logg},
#  year = {2017},
#  publisher = {Springer},
#  doi = {10.1007/978-3-319-52462-7},
#  isbn = {978-3-319-52461-0},
# }

#Import packages
from dolfin import *
import matplotlib.pyplot as plt
from mshr import *
import numpy as np
import csv
import pandas as pd

#=============================================================================
#Begin Script
#=============================================================================
#Define Variables
D = 3600*1.6E-11            #Dispersion coefficient (m2/hr)
h = 10                      #Vertical plume thickness (m)
Q = 0.0138*3600             #Injection rate (m3/hr)
n = 0.33                    #porosity
c_i = 1000                  #initial particle concentration (g/m3)
r_inflow = 0.2              #inflow pipe radius
v_i = Q/(2*3.1415*n*h*r_inflow)  #initial plume flow velocity
dp = 10E-6                  #particle diamater (m)
dc = 75E-6                  #collector diameter (m)
A = 7.8E-20                 #Hamaker Constant
k = 1.3805E-23              #Boltzmann Constant
T = 350                     #Absolute fluid temp (K)
ap = dp/2                   #particle radius (m)
mu = 0.00005                #fluid viscosity (Pa*s) - dependent on temp and pressure ******
D_inf = k*T/(6*pi*mu*ap) #Diffusion in infinite medium
rho_p = 2.9E6               #particle density (g/m^3)
rho_f = 0.5E6               #fluid density (g/m^3) - dependent on temp and pressure *******
alpha = 0.018               #attachment efficiency
t=0

header = ['Dispersion Coefficient (m2/s)', 'Flow Rate (m3/s)', 'Porosity', 'Inflow Concenctration (g/L)', \
        'Particle Diameter (microns)', 'Grain Size (microns)', 'Hamaker Constant (J)', 'Temperature (K)', 'Viscosity
(Pa*s)', Fluid Density (g/cm3)', 'Alpha', 'D50 (m)']

data = [D/3600, Q/3600, n, c_i/1000, dp*1000000, dc*1000000, A, T, mu, rho_f/1000000, alpha]
```

```
#=========================================================================
#Create Mesh
T = 48
end = (pow(Q*T/3.1415/h/n, 0.5))              #how far flow  will travel in time T
mesh_res = 25                          #how many mesh lines
domain = Circle(Point(0, 0), Constant(end)) - Circle(Point(0,0), Constant(r_inflow))
mesh = generate_mesh(domain, mesh_res)
num_steps = 24           #Number of time steps
dt = T / num_steps        #Size of each time step (hours)

#Define Function Space based on mesh
V = FunctionSpace(mesh, 'P', 2)

#Define trial and test functions
c = TrialFunction(V)
y = TestFunction(V)

#=========================================================================

#Expressions for radius, porosity, and flow velocity
r = Expression('pow(x[0]*x[0]+x[1]*x[1], 0.5)', degree=2)  #radius as function of position
vel = Expression('Q/(2*3.1415*n*h*r)', degree=1, Q=Q, n=n, h=h, r=r)
gamma = Expression('pow((1-n),0.333)', degree=1, n=n)
D = Expression('D*vel', degree=1, D=D, vel=vel)

#Unitless params
A_s = Expression('(2*(1-pow(gamma,5)))/(2-3*gamma+3*pow(gamma,5)-2*pow(gamma,6))', degree=1,
gamma=gamma)
N_r = dp/dc  #Aspect ratio
N_pe = Expression('vel*dc/D_inf', degree=1, vel=vel, dc=dc, D_inf=D_inf)  #Peclet Number
N_vdw = A/k/T  #van der Waals Number
N_a = Expression('A/(12*pi*mu*ap*ap*vel)', degree=2, A=A, pi=pi, mu=mu, ap=ap, vel=vel)  #Attraction number
N_g = Expression('2/9*ap*ap*(rho_p-rho_f)*9.81/mu/vel', degree=2, ap=ap, rho_p=rho_p, rho_f = rho_f, mu=mu,
vel=vel)

#Calculating eta
n_D = Expression('2.4*pow(A_s,0.333)*pow(N_r,-0.081)*pow(N_pe,-0.715)*pow(N_vdw,0.052)', \
    degree=1, A_s=A_s, N_r=N_r, N_pe=N_pe, N_vdw=N_vdw)  #Diffusion

n_I = Expression('0.55*A_s*pow(N_r, 1.675)*pow(N_a, 0.125)', \
    degree=1, A_s=A_s, N_r=N_r, N_a=N_a)  #Interception

n_G = Expression('0.22*pow(N_r,-0.24)*pow(N_g, 1.11)*pow(N_vdw,-0.052)', \
    degree=1, N_r=N_r, N_g=N_g, N_vdw=N_vdw)  #Gravitation

n_0 = Expression('n_D + n_I + n_G', degree=1, n_D=n_D, n_I=n_I, n_G=n_G)
ka = Expression('alpha*n_0', degree=1, alpha=alpha, n_0=n_0)
```

```
#=======================================================================
#Define Boundary Conditions
#Inflow with radius given by inflow pipe radius
def inf_boundary(x, on_boundary):
   return on_boundary and pow(x[0]*x[0]+x[1]*x[1], 0.5) <= (r_inflow + 0.01)

#External boundary based on flow rate and time
def ext_boundary(x, on_boundary):
   return on_boundary and pow(x[0]*x[0]+x[1]*x[1], 0.5) >= (end - 0.1)

bc_i = DirichletBC(V, Constant(c_i), inf_boundary)     #Constant concentration at inflow
#bc_f = DirichletBC(V, Constant(0), ext_boundary)      #Zero concentration at extreme boundary
#bcs = [bc_i, bc_f]
c_n = interpolate(Constant(c_i), V)                  #Define value for previous timestep

#=======================================================================

#Define Functions
a = D*dt*dot(grad(c), grad(y))*dx - (vel*c*dt + c)*y*dx  #Left side of equation
L = (ka*c_n*dt - c_n - vel*c_n*dt)*y*dx               #Right side of equation

#Solve with time steps
c = Function(V)

for x in range(num_steps):
   #Update time
   t += dt
   #Solve
   solve(a==L, c, bc_i)

   #Expressions for  porosity and flow velocity
   n_n = n
   n = Expression('n_n*(1-n_n*(c_n-c)/rho_p)', degree=1, rho_p=rho_p, c_n=c_n, c=c, n_n=n_n)
   vel = Expression('Q/(2*3.1415*n*h*r)', degree=1, Q=Q, n=n, h=h, r=r)
   gamma = Expression('pow((1-n),0.333)', degree=1, n=n)
   c_n.assign(c)         #Update concentration for previous timestep

   #Unitless params
   A_s = Expression('(2*(1-pow(gamma,5)))/(2-3*gamma+3*pow(gamma,5)-2*pow(gamma,6))', degree=1,
   gamma=gamma)
   N_r = dp/dc  #Aspect ratio
   N_pe = Expression('vel*dc/D_inf', degree=1, vel=vel, dc=dc, D_inf=D_inf)  #Peclet Number
   N_vdw = A/k/T  #van der Waals Number
   N_a = Expression('A/(12*pi*mu*ap*ap*vel)', degree=2, A=A, pi=pi, mu=mu, ap=ap, vel=vel)  #Attraction number
   N_g = Expression('2/9*ap*ap*(rho_p-rho_f)*9.81/mu/vel', \
        degree=2, ap=ap, rho_p=rho_p, rho_f = rho_f, mu=mu, vel=vel) #Gravity number

   #Calculating eta
   n_D = Expression('2.4*pow(A_s,0.333)*pow(N_r,-0.081)*pow(N_pe,-0.715)*pow(N_vdw,0.052)', \
    degree=1, A_s=A_s, N_r=N_r, N_pe=N_pe, N_vdw=N_vdw)  #Diffusion

   n_I = Expression('0.55*A_s*pow(N_r, 1.675)*pow(N_a, 0.125)', \
    degree=1, A_s=A_s, N_r=N_r, N_a=N_a)  #Interception
```

```
    n_G = Expression('0.22*pow(N_r,-0.24)*pow(N_g, 1.11)*pow(N_vdw,-0.052)', \
      degree=1, N_r=N_r, N_g=N_g, N_vdw=N_vdw)    #Gravitation

    n_0 = Expression('n_D + n_I + n_G', degree=1, n_D=n_D, n_I=n_I, n_G=n_G)
    ka = Expression('alpha*n_0', degree=1, alpha=alpha, n_0=n_0)

#=============================================================================

#Plot Results (color map)
p = plot(c, title = 'Particle Concentration (g/m3)')
p.set_cmap('viridis')
p.set_clim(0.90, c_i)
plt.colorbar(p)
plt.xlabel('Meters')
plt.savefig('a'+str(alpha)+'.png')
plt.close()

#Line plot
x = np.linspace(.201, end-.001, 50)     #start, stop, number of points
points = [(x_, 0) for x_ in x]                #loop through each point along axis
c_line = np.array([c(point) for point in points])
plt.plot(x, c_line, color='g')
plt.xlabel('Distance from inflow (m)')
plt.ylabel('Particle Concentration (g/m3)')
plt.savefig('line_a'+str(alpha)+'.png')
for point in points:
    if c(point) <= 0.9*c_i:
        dist=point[0].round(2)
        data.append(dist)
        break
```